

Mini AuAg Wavy Nanorods Displaying Plasmon-Induced Photothermal and Photocatalytic Properties

Javier Quintana, Julián Crespo, Andrea Falqui, José M. López-de-Luzuriaga, M. Elena Olmos, María Rodríguez-Castillo,* and Miguel Monge*

Alloyed AuAg wavy nanorods (wNRs) of ≈ 24.0 nm length and 3.5 nm width are formed by the mild decomposition of the organometallic complex $[\text{Au}_2\text{Ag}_2(\text{C}_6\text{F}_5)_4(\text{OEt}_2)_2]_n$ in tetrahydrofuran (THF) in the presence of oleic acid. Ligand exchange with L-glutathione (GSH) or poly(ethylene glycol) methyl ether thiol (PEG-SH) leads to water-soluble nanostructures. These AuAg wNRs display tunable size-dependent longitudinal localized surface plasmon resonance (L-SPR) broad absorptions beyond 750 nm in the near-infrared (NIR) I and II regions. These intense plasmonic absorptions lead to interesting photothermal, catalytic, and photocatalytic properties, including the catalytic reduction of 4-nitrophenol, the photocatalytic reduction of 4-nitrostyrene, or the photocatalytic dehydrogenation of ammonia borane for H_2 release.

1. Introduction

1D noble metal nanorods (NRs) are one of the most promising nanomaterials due to their plasmonic properties,^[1,2] which can be tuned mainly through a delicate control of their dimensions. The importance of these materials is reflected in a wide range of successful applications such as bio- and chemosensing,^[3,4] optical data storage,^[5] photothermal cancer treatment,^[6] catalysis,^[7] or photocatalysis.^[8]

Upon interaction of light with rod-shaped noble metal nanoparticles, these manifest two surface plasmon resonance (SPR) absorptions, i.e., a transverse one (t-SPR) and a longitudinal one (l-SPR), being the latter tuneable in a wide range from

the visible (up to 700 nm) to the near-infrared (NIR) I (700–900 nm) or, even, to the NIR II (1000–1700 nm) range.^[9,10] The most usual way of tuning this l-SPR absorption is the modification of the NRs aspect ratio. Nevertheless, an even tighter mastering of this l-SPR absorption could be exerted by a combined control of the composition, the size (aspect ratio), and the shape leading, even, to enhanced or new properties.


Among the different types of noble metal nanoparticles, composition controlled bimetallic ones formed by the combination of gold and silver display remarkable stability and tailored plasmonic or catalytic properties compared with

the corresponding monometallic constituents.^[11] In the case of bimetallic AuAg NRs obtained through wet-chemical approaches, a main class of nanostructure is described, i.e., Au@Ag core-shell NRs, being the AuAg alloyed NRs much less represented.^[1] The facile formation of the core-shell structure, in spite of the ease phase segregation between gold and silver, arises from the smaller surface energy value of silver with respect to gold.^[12] A number of works have described the controlled annealing of core-shell AuAg NRs to afford the synthesis of alloyed ones when the nanostructures are covered with a SiO_2 shell, although in the absence of such protection the annealing of anisotropic nanostructures may lead to isotropic spherical ones.^[13–15] Therefore, the direct synthesis of alloyed AuAg rod-shaped nanostructures is a challenging issue. Moreover, the interest on this type of bimetallic AuAg NRs stems from their versatility in potential applications. This type of nanostructures has been used, for instance, in surface enhanced Raman scattering for the monitoring of catalytic oxidation and reduction reactions using AuAg porous alloy NRs^[16] and for the detection of Rhodamine 6G in surface wastewater using AuAg NRs@ SiO_2 ,^[17] or the improved detection of 4-nitrothiophenol employing Au NR@AuAg shell.^[18]

In addition to composition, the size (aspect ratio) control of colloidal noble metal NRs or nanowires (NWs) provides a fundamental tool for plasmonic tuning. For example, ultrathin Au^[19] and AuAg^[20] NRs (UNRs) and NWs (UNWs) displaying diameters of less than 2 nm and lengths from several nm to μm give rise to notably redshifted l-SPR absorptions up to the far-IR (Au UNWs) or mid-IR (AuAg UNWs), probably due to the increase of the dielectric constant arising from the ultrathin nature of the nanostructures.^[21] The special characteristics of

J. Quintana, J. Crespo, J. M. López-de-Luzuriaga, M. E. Olmos, M. Rodríguez-Castillo, M. Monge
Departamento de Química, Centro de Investigación en Síntesis Química (CISQ)
Universidad de La Rioja Complejo Científico-Tecnológico
26006 Logroño, Spain
E-mail: maria.rodriguez@unirioja.es; miguel.monge@unirioja.es

A. Falqui
Department of Physics “Aldo Pontremoli”
University of Milan
Via Celoria 16, 20133 Milan, Italy

 The ORCID identification number(s) for the author(s) of this article can be found under <https://doi.org/10.1002/adpr.202200246>.

© 2022 The Authors. Advanced Photonics Research published by Wiley-VCH GmbH. This is an open access article under the terms of the Creative Commons Attribution License, which permits use, distribution and reproduction in any medium, provided the original work is properly cited.

DOI: 10.1002/adpr.202200246

these materials have permitted the application of Au UNWs as stable pressure sensors showing high sensitivity.^[22] Other interesting examples of size-controlled noble metal NRs are mini Au NRs (diameter of less than 10 nm), which display tuneable plasmonic properties in the visible–NIR region, leading to extremely efficient photothermal properties.^[23] However, the tuning of the plasmonic properties of mini NRs is difficult because the increase in length usually leads to diameter increase in this mini-size regime, what makes the development of new synthetic approaches for this type of nanostructures a very interesting idea.

A third factor affecting the tuning of the plasmonic properties of rod-shaped noble metal nanoparticles is the shape control. This is usually achieved through NRs overgrowth. At this regard, Song et al. recently reported on the DNA-mediated Au NRs reshaping from nanodumbbells to nanooctahedra, leading to the control of the l-SPR absorptions beyond 1000 nm, in the NIR II region. The large redshift of the l-SPR absorption is related to the narrower diameter of the middle region of the nanostructures.^[24] Also, Zhang et al. reported on the overgrowth of Au NRs into concave and convex nanocuboids or nanocubes, achieving a broad redshift of the l-SPR in the case of the former ones.^[25] Regarding AuAg bimetallic rod-like nanostructures, AuAg NRs and NWs were prepared by diffusing AgCl into preformed Au NRs, leading to the corresponding t-SPR and l-SPR absorptions.^[26] However, a direct one-step shape control of rod-like noble metal nanostructures leading to efficient l-SPR absorptions in the NIR region has not been reported to date.

In addition to the singularity of the morphology and surface plasmon resonance tuning that can be achieved when a tight control of composition, size, and shape is applied, the new nanostructures would provide a combination of characteristics that make them ideal for improved applications. At this regard, the confluence of three interesting properties such as 1) catalytic activity; 2) surface plasmon-induced photothermal heating and 3) NIR light generation of hot electrons, within a given type of nanostructure, would provide a very promising platform for light-to-energy conversion applications.

We have previously reported on the synthesis of alloyed AuAg spherical nanoparticles^[27] or ultrathin 1D NWs (UNWs) and straight NRs (UNRs)^[20] displaying localized surface plasmon resonance (LSPR) absorptions in the visible (spherical), or in the NIR and mid-IR (UNRs and UNWs) regions. To achieve the synthesis of the ultrathin AuAg NWs and NR materials, we carried out the mild decomposition of the organometallic complex $[Au_2Ag_2(C_6F_5)_4(OEt)_2]_n$ using pure oleic acid (OA) as solvent,

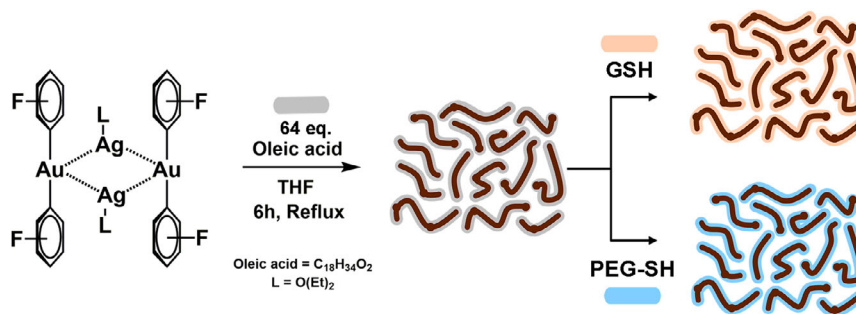
capping ligand, and growth-directing agent. Herein, we report a straightforward and consistent organometallic approach for the synthesis of 1D rod-like nanostructures displaying alloyed composition (AuAg), small size (mini rod-like), and complex shape (wavy nanorods, wNRs). This singular one-step approach of combined control of size, shape, and composition provides nanostructures displaying very intense and tuneable plasmonic absorptions in the NIR II region (1000–1700 nm). We have proved the ligand exchange possibilities on these AuAg wNRs transforming hydrophobic wNRs into hydrophilic ones, keeping the morphology and plasmonic properties. Remarkably, these AuAg wNRs lead to interesting catalytic and plasmonic-induced photothermal and photocatalytic properties, including NIR-induced plasmonic photocatalytic reduction of 4-nitrostyrene or photocatalytic hydrolysis of ammonia borane for H₂ release.

2. Results and Discussion

2.1. Synthesis and Characterization of AuAg wNRs

The synthesis of OA-AuAg wNRs (1) was carried out by the controlled reduction of complex $[Au_2Ag_2(C_6F_5)_4(OEt)_2]_n$ (Scheme 1) under argon atmosphere, in the presence of 64 equivalents of OA and using anhydrous tetrahydrofuran (THF) as solvent. The light-protected reaction mixture was stirred for 6 h under reflux leading, in all cases, to the formation of a dark red solution, due to the combination of a main population of AuAg NRs and spherical nanoparticles. The solvent was removed under vacuum and the solid obtained was washed by centrifugation with toluene:ethanol mixtures, to isolate a dark brown solution of purified OA-AuAg wNRs (1).

Figure 1A depicts the corresponding transmission electron microscopy (TEM) image of OA-AuAg wNRs (1) of 24 ± 9 nm length, 3.5 ± 0.5 nm width, and wavy shape. Figure 1B shows the high-resolution transmission electron microscopy (HRTEM) micrograph for OA-AuAg wNRs (1). The HRTEM analysis (see Figure 1B and S1, Supporting Information) indicates that the OA-AuAg wNRs display fcc lattice parameters expected for gold or silver. The wNRs grow along the (111) direction, although some deviations from a straight growth, leading to the wavy shape, could arise from defects and/or local changes in the crystalline orientation. To characterize the alloy composition of the AuAg wNRs, we collected high-angle annular dark-field scanning transmission electron microscopy (STEM-HAADF) images and the corresponding energy-dispersive X-Ray



Scheme 1. Synthesis of AuAg wNRs and replacement of capping ligands.

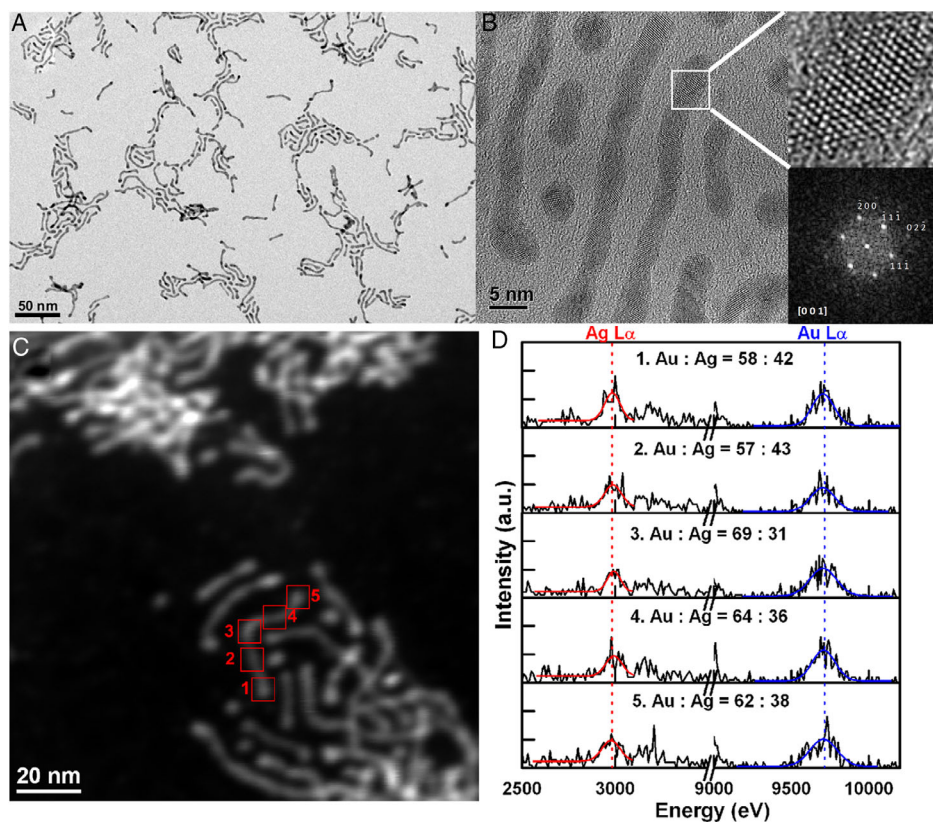


Figure 1. A) TEM image of OA-AuAg wNRs (1); B) HRTEM image of a crystalline OA-AuAg wNR (1), numerical diffractogram of the AuAg wNR (1) ([001] zone axis of the gold/silver lattice) and magnification of the squared area; C) STEM-HAADF image of a group of AuAg wNRs (1); and D) EDS spectra of different parts (1–5 in STEM-HAADF image) of a single wNR, with corresponding Au:Ag ratio obtained by Gaussian fits of the L α peaks of Ag (centered at 2.984 keV) and Au (centered at 9.712 keV).

spectroscopy (EDS) analysis of OA-AuAg wNRs (1). This analysis shows a higher gold composition, with Au:Ag ratio of $\approx 60:40$ (see Figure 1C,D).

On the other hand, the capping OA molecules can be replaced by new stabilizing agents (Scheme 1), which allow the dissolution of the wNRs in water. Thus, a THF solution of the obtained nanoparticles was mixed with a water solution of L-glutathione (GSH) or poly(ethylene glycol) methyl ether thiol (PEG-SH) during 30 min. Then, the organic solvent was removed under vacuum and the resulting brown water solution was lyophilized during 2 days, resulting a dark brown solid corresponding to

GSH-AuAg wNRs (2) and PEG-SH-AuAg wNRs (3), respectively. **Figure 2A,B** displays the TEM images of AuAg wNRs (2) and (3) with lengths of 23 ± 8 and 24 ± 10 nm, respectively. These wNRs (2 and 3) show similar dimensions to those of the starting wNRs 1, showing the possibility of exchange of the stabilizing species without altering the morphology of the AuAg nanostructures. This exchange permits broadening the study of properties and potential applications of these wNRs in aqueous media and, moreover, the storage and handling of solid samples of wNRs are favored when large excesses of GSH or of PEG-SH are used.

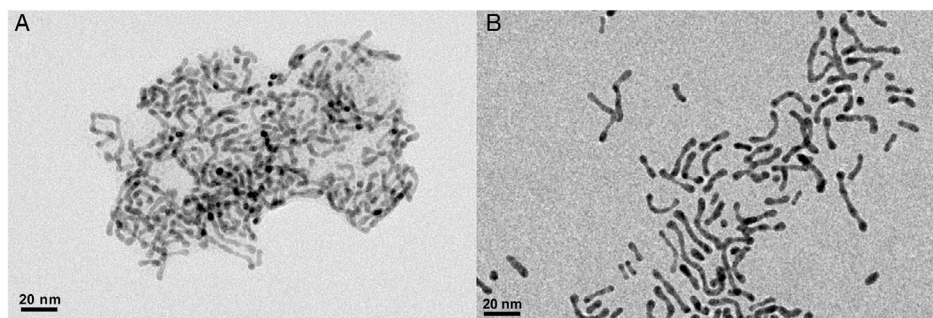


Figure 2. TEM image of A) GSH-AuAg wNRs (2); B) PEG-SH-AuAg wNRs (3).

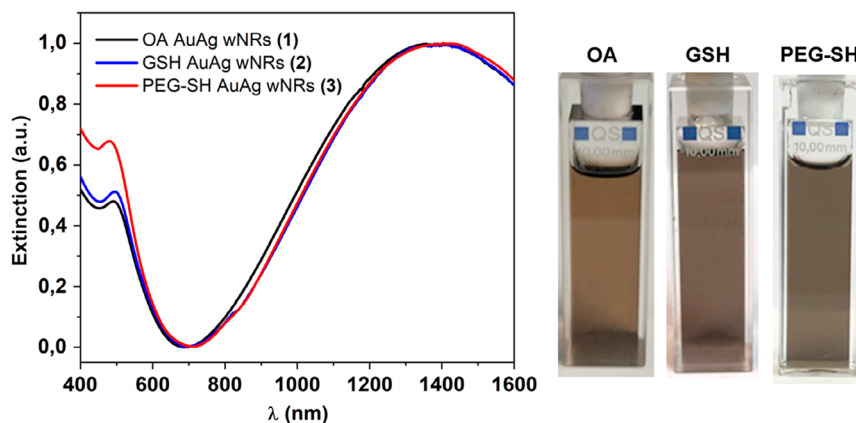


Figure 3. UV-vis spectra and DMSO solutions of AuAg wNRs (1-3).

The plasmonic properties of AuAg wNRs are similar for samples 1–3, in agreement with their similar morphology (**Figure 3**), showing a strong absorption in the NIR II region, with a maximum around 1400 nm. This strong absorption arises from the longitudinal mode of the surface plasmon resonance (l-SPR) of the wNRs. In addition, these nanostructures display a less intense absorption due to the transverse mode (t-SPR), with a maximum around 500 nm, which is not suppressed as it occurs for similar ultrathin AuAg UNRs with diameters of less than 2 nm.^[20]

It is worth to highlight the importance of the OA in this synthetic approach because it not only acts as a capping ligand for the final nanostructures, but also as a growth-directing agent at the molecular level that will determine the shape and aspect ratio of the new wNRs. Indeed, we can obtain an excellent control of the AuAg wNRs aspect ratio by varying the OA:metal precursor ratio. The results of this control can be observed in **Figure 4**, where TEM images of AuAg wNRs obtained through the decomposition of bimetallic Au(I)–Ag(I) complex are shown. In these experiments, a fixed concentration of the organometallic precursor was used, in the presence of different ratios of OA: 32 (**Figure 4A**, AuAg wNRs (4)), 96 (**Figure 4B**, AuAg wNRs (5)), 128 (**Figure 4C**, AuAg wNRs (6)), and 256 (**Figure 4D**, AuAg wNRs (7)). The analysis of these images indicates that the nanostructures display a similar width between 3 and 5 nm, while the lengths increase with the amount of OA, with an average of 23 ± 9 nm (4), 24 ± 9 nm (1), 26 ± 8 nm (5), 29 ± 11 nm (6), and 31 ± 10 nm (7) (see **Figure S2**, Supporting Information). The increased aspect ratio allows a good tuning of the l-SPR plasmonic absorption in the NIR II region, as observed in **Figure 4E**, leading to a redshift of this l-SPR mode. When the OA:AuAg molar ratio is represented versus the NIR II absorption maximum, a linear correlation is obtained (**Figure 4F**). Addition of very large excess of OA leads to the formation of spherical OA-AuAg nanoparticles (8). A similar redshift of the l-SPR absorption has been previously reported for alloyed AuAg NRs of larger length and diameter,^[13] displaying comparable l-SPR absorptions between ≈ 1125 and 1740 nm for aspect ratios between 5 and 9 and for NRs width of ≈ 40 nm. In our case, the mini AuAg wNRs display l-SPR absorptions between 1350 and 1720 nm for aspect ratios between 4.8 and 9 and for

wNRs width between ≈ 3 and 5 nm. Although there is not a complete match between the absorption maxima for nanostructures of similar aspect ratio, there is a similar range of l-SPR absorptions, specially taking into account their broadness. On the other hand, a comparison can be also established with other types of mini (diameter less than 10 nm) gold-based anisotropic nanostructures displaying l-SPR absorptions beyond 1000 nm as, for instance, mini Au NRs^[23] and ultrathin Au^[19] or AuAg^[20] NRs (UNRs). In the case of mini Au NRs, the l-SPR absorptions appear between 793 and more than 1300 nm for aspect ratios between 3.8 and 10.8 and for NRs width between 5.5 and 8.7 nm. In the case of oleylamine capped Au UNRs, the l-SPR absorptions appear between 1320 and more than 2300 nm for aspect ratios between 2.6 and 15 and for UNRs width between 1.6 and 2 nm. Finally, in the case of OA capped AuAg UNRs, the l-SPR absorptions appear between 1705 and 2205 nm for aspect ratios between 12.5 and 19.7 and for UNRs width between 1.9 and 2.1 nm. Taking into account these observations, there is, in all cases, a clear relationship between the increasing aspect ratio and the l-SPR wavelength redshift. Indeed, if one observes the width of each type of nanostructure, a more pronounced redshift can be observed in the case of ultrathin Au and AuAg UNRs, with diameters below 2 nm, that is also concomitant with the suppression of the t-SPR band. Then, an intermediate redshift for the AuAg wNRs reported in the present study is registered, with diameters between 3 and 5 nm and, finally, a less pronounced redshift for mini Au NRs with diameters between 5.5 and 8.7 nm is obtained. This tendency would be in agreement with previous studies by Yu et al.^[28] in which larger negative values of the resonant permittivity (ϵ_r) were calculated with increasing aspect ratios. In the limit of the ultrathin plasmonic nanostructures, very pronounced redshifts of the l-SPR to the mid-IR region have also been observed. This was reported by some of us for AuAg UNWs, which display very broad l-SPR with a maximum at 6500 nm for aspect ratios between 18 and 47, with UNWs lengths between 35 and 90 nm and 1.9 nm width.^[20] Therefore, the ultrathin nature in the latter case would have an important influence in the larger negative values of the resonant permittivity (ϵ_r), as previously reported for Au UNRs and UNWs.^[19] It is important to note that in the case of the AuAg wNRs reported here, the influence of the alloyed nature of the

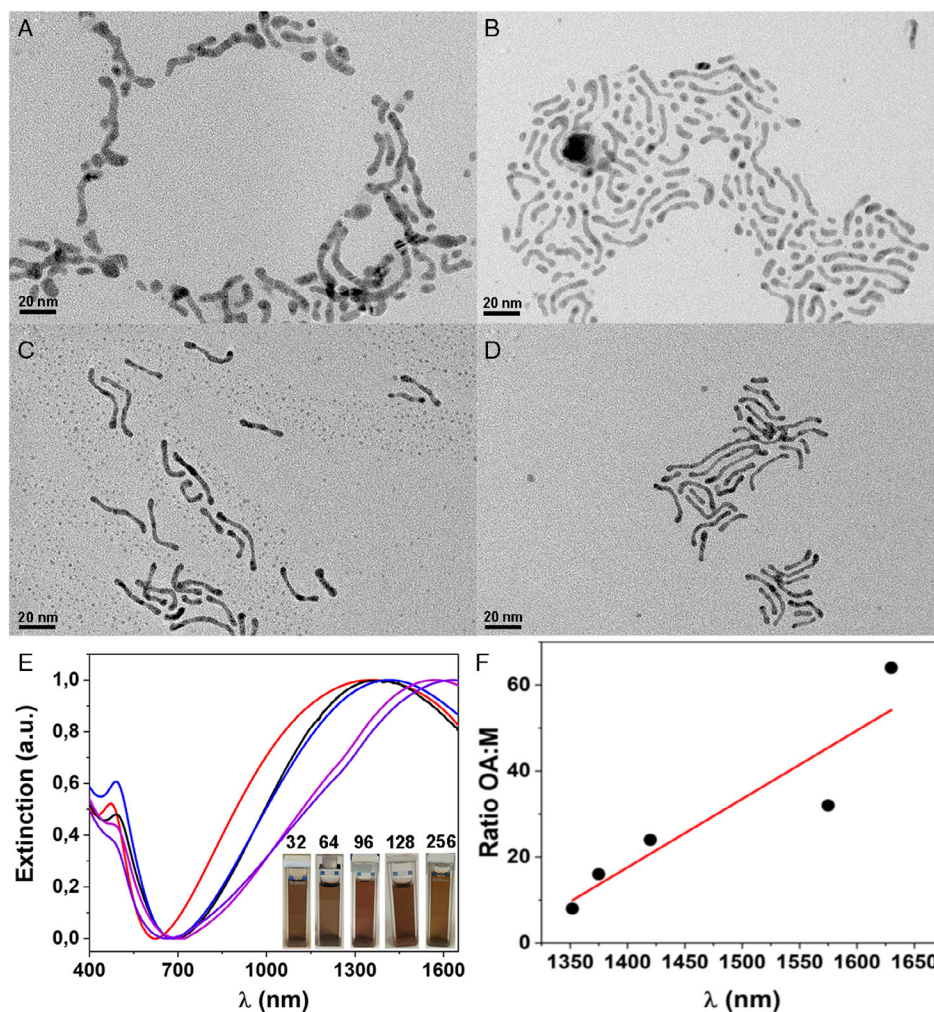


Figure 4. A–D) TEM images of OA-AuAg wNRs (4–7); E) normalized UV/vis/NIR spectra of AuAg NRs (1, 4–7) (THF); F) absorption maximum versus length of AuAg NRs.

nanostructures, the wavy shape, and the wNRs widening in the tips or along the structure (vide infra) in the l-SPR wavelength absorption could not be excluded.

It is worth mentioning that in the images reported in Figure 1, 2, and 4 the AuAg wNRs usually display widening on the tips and/or within the wNRs structure. This could be attributed to the formation of spherical AuAg NPs acting as seeds from which the AuAg wNRs start to grow, although the case of AgAg spherical NPs welding cannot be ruled out because the widening of the wNRs is also observed within the nanostructure and not only on the tips. This mechanism is also supported by the fact that the diameter of the initially formed spherical AuAg NPs is slightly larger than the AuAg wNRs width. Indeed, Figure S3, Supporting Information, depicts HRTEM images displaying different stages of possible oleic acid-assisted attachment or cold welding processes between AuAg spherical NPs, leading to different degrees of surface diffusion of Au and Ag atoms even at room temperature. This observation is similar to the one proposed by Xia and co-workers for wavy Au NWs.^[29] Alternatively, the OA-directed deposition of Au and Ag atoms arising from the

reduction of remaining organometallic precursor leading to the anisotropic growth cannot be discarded.

In order to support this observation, we carried out a time-monitored UV–vis–NIR absorption study, i.e., acquiring several corresponding spectra during the formation of OA-AuAg wNRs (1) after 60, 120, 240, and 360 min (see Figure S4, Supporting Information). After 60 min of reaction, the only LSPR absorption observed at ≈ 500 nm points to the presence of only small sized AuAg spherical NPs because the absence of l-SPR absorptions in the NIR region allows, ruling out the formation of wNRs from the beginning of the reaction. After 120 min, the LSPR absorption appears slightly redshifted to 505 nm and more intense, together with an incipient broad absorption between 800 and 1400 nm, corresponding to the l-SPR mode related to the formation of some amount of anisotropic AgAg wNRs. After 240 and 360 min of reaction, both SPR absorptions become more evident, indicating the formation of a large amount of AuAg wNRs. The fact that the high energy absorption at 512 nm is very intense indicates the presence of both spherical NPs and wavy NRs, being the former separated in the experimental workup.

In addition, the broadness of the L-SPR absorption does not permit to propose whether the aspect ratio of the wNRs increased after each measurement. Overall, the time-monitored measurements and the electron microscopy observations would support the waviness of the AuAg anisotropic nanostructures. The attachment or the welding of AuAg spherical NPs with different orientations would be responsible of such uncommon way shape.

X-ray photoelectron spectroscopy (XPS) analyses were performed to gain insight into the surface elemental composition and the elemental chemical states of the atoms forming the solid samples of GSH-AuAg wNRs (2) and PEG-SH-AuAg wNRs (3) (see Figure 5 and S5, Supporting Information, for XPS spectra for wNRs 2 and 3). The description of the wide spectra for 2 and 3 and the detailed analysis of the high-resolution spectra obtained for GSH-AuAg wNRs (2) are described in Supporting Information.

The experimental signals of the high-resolution XPS spectrum for the Au 4*f* region of PEG-SH-AuAg wNRs (3) are fitted to two spin-orbit doublets of different intensity and equally separated in energy (≈ 3.7 eV). The lower energy intense doublet at 83.9 and 87.6 eV can be assigned to Au⁰; meanwhile, the less intense doublet at 84.4 and 88.1 eV is related to the presence of gold atoms in +1 oxidation state. The presence of Au⁺ could be attributed to low coordination number atoms at the surface of the small size (sub-10 nm diameter) wNRs.^[30,31]

In the case of the high-resolution XPS spectrum for the Ag 3*d* region of 3, again two experimental signals fitted to two spin-orbit doublets (energy separation of ≈ 6.0 eV) are obtained.

Metallic silver (Ag⁰) can be assigned to the peaks at 367.6 and 373.6 eV. The peaks at 368.2 and 374.1 eV can be ascribed to the presence of Ag(I) for a similar reason to that described for Au.^[32]

The high-resolution XPS spectrum for the C 1*s* region for 3 is fitted into one intense peak and three weak ones. The intense peak at 286.3 eV can be assigned to the C–O bonds present in the polyethylene glycol polymer. The low energy deconvoluted peak at 284.8 eV is related to C–C bonds; meanwhile, the less intense peaks at 287.1 and 288.2 eV could be associated to –C=O and –COOH groups of a small amount of remaining OA at the surface of the wNRs.^[33] In addition, the high-resolution spectrum of the S 2*p* region provides a very weak peak that can be fitted into two signals at 163.9 and 165.8 eV corresponding to C–S and S–H bonds, respectively.^[34]

2.2. NIR-Induced Photothermal Heating

The generation of thermal energy through the plasmonic absorption of NIR irradiation, i.e., photothermal effect, is one of the most interesting properties of plasmonic gold-based anisotropic nanostructures. In this sense, the broad and intense longitudinal plasmonic absorptions displayed by the AuAg wNRs reported in this work within the 750–1700 nm range make them excellent candidates for their use in photothermal applications. To test their possible uses, we studied first the photothermal temperature increase produced when AuAg wNRs were irradiated using two different low-power light-emitting diode (LED) sources of

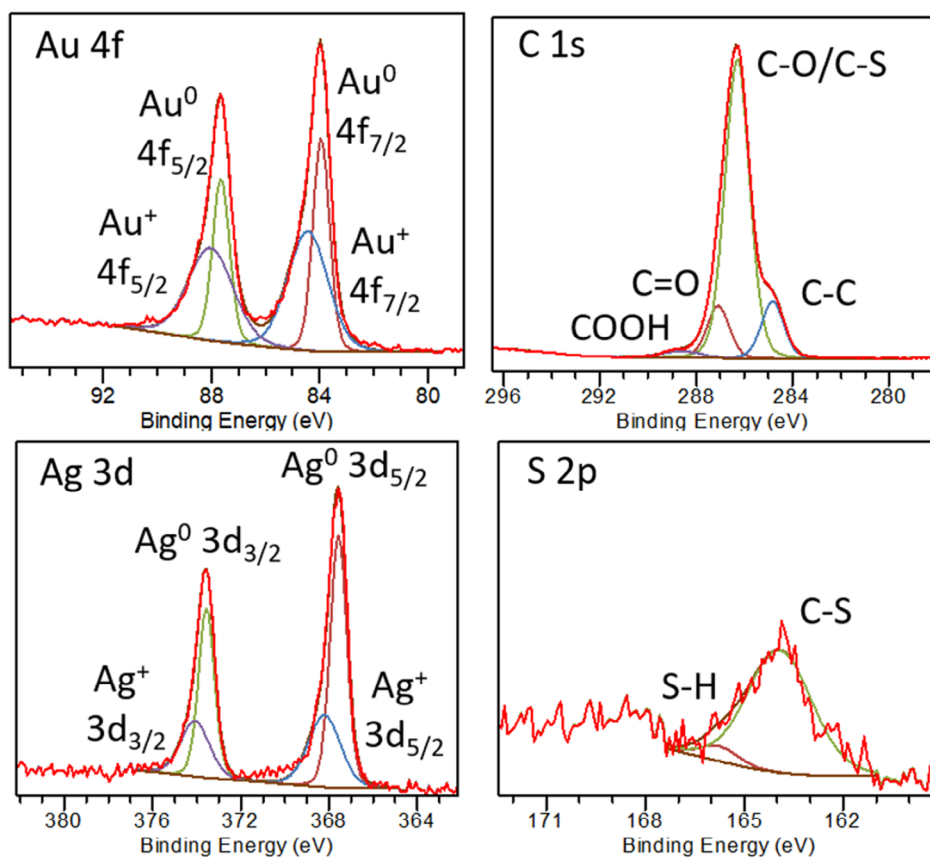


Figure 5. High-resolution XPS spectra for Au 4*f*, Ag 3*d*, C 1*s*, and S 2*p* for PEG-SH AuAg wNRs (3).

850 and 940 nm (3.2 W cm^{-2}), using a thermographic camera for the detection of the temperature increase.

Figure 6A depicts the photothermal heating of a sample of PEG-SH-AuAg wNRs (3) in water solution (3.3 mg mL^{-1} of wNRs). The results show an increase of the temperature up to 43°C when a 850 nm NIR LED was used (25°C for water blank) or up to 62°C when a 940 nm NIR LED was used (32°C for water blank). The photothermal heating-cooling cycles for PEG-SH-AuAg wNRs (3) in water are shown in **Figure 6B**. **Figure 6C** shows the photothermal heating of a poly(methylmethacrylate) (PMMA) film charged with OA-AuAg wNRs (1). For this, a solution of similar concentration to the previous one in dichloromethane as solvent and in the presence of 25 mg of PMMA was prepared. The solution was deposited on a quartz substrate, leading to a homogeneous film after solvent evaporation. The irradiation of these films, where a high surface concentration of AuAg wNRs is achieved, led to a fast and significant photothermal temperature increase up to 76°C when the 850 nm LED was used and up to 130°C when the 940 nm LED was employed. For both solution and PMMA films, the irradiation with the lower energy 940 nm NIR LED gives rise to higher temperatures due to the much more intense I-SPR absorption found for these nanostructures at this wavelength. We have checked that the OA-AuAg wNRs (1) shape is not kept when they are irradiated with NIR LED light for some minutes. Instead, an entanglement of wNRs is observed, leading to an even broadened I-SPR absorption. However, the shape and plasmonic properties of the PEG-SH-AuAg wNRs (3) are almost kept after irradiation, whereas PMMA films of OA-AuAg wNRs (1) confer a very good protection toward NIR LED light irradiation because the shape and plasmonic properties of AuAg wNRs are fully kept after NIR irradiation (see **Figure S6–S9**, Supporting Information).

Interestingly, PEG-SH-AuAg wNRs (3) can be employed as a very efficient nanoheater in the purification of water via steam generation, by using 940 nm NIR LED irradiation: for this, we measured the weight loss of water from a 3.3 mg mL^{-1} solution of 3 in a quartz cuvette and we compared the result with the irradiation of water (see **Figure S10**, Supporting Information). The irradiated solution of 3 lost $\approx 300 \text{ mg}$ of steam water in 60 min at a $5.3 \text{ mg cm}^{-2} \text{ min}^{-1}$ rate (linear fit) and reaching a temperature of 62°C , whereas the pure water sample lost $\approx 60 \text{ mg}$ of steam water in 60 min, at a $1.0 \text{ mg cm}^{-2} \text{ min}^{-1}$ rate (linear fit) and reaching 32°C . This promising result is

comparable to that reported for plasmonic gold colloidosomes that produced a loss of $\approx 425 \text{ mg}$ of steam water in 30 min ($\approx 14.2 \text{ mg cm}^{-2} \text{ min}^{-1}$ rate), but using a broad-range irradiation between 400 and 1000 nm, representing the solar spectrum, instead of the monochromated low-power NIR LED light of 940 nm.^[35] At this regard, there is an increasing interest in the immobilization of plasmonic nanostructures on 2D surfaces for the design of improved heterostructured materials with application in water steam generation. For example, Au NRs have been assembled in cellulose biofoams leading to a highly efficient steam generation system producing $19.2 \text{ mg cm}^{-2} \text{ min}^{-1}$ of water steam when the material was irradiated with a 808 nm laser source of 1.3 W cm^{-2} , and reaching a macroscopic photothermal heating of 48°C .^[36] In another report by Wu et al., a novel photothermal material based on Au nanocages (NCs) incorporated into poly(vinylidene fluoride) (PVDF) electrospun nanofibers was described.^[37] This material efficiently harvests NIR light (808 nm laser, 0.4 W cm^{-2}) leading to an increase in temperature up to 96°C and a water steam generation rate of $6.1 \text{ mg cm}^{-2} \text{ min}^{-1}$. Also, in a recent report, a new heterostructure composed by Au NRs and 2D graphene oxide (GOx) nanosheets was used for photothermal steam generation by irradiation with a NIR laser (808 nm, 0.1 W cm^{-2}). This material leads to a steam generation rate of $2.23 \text{ mg cm}^{-2} \text{ min}^{-1}$ at a maximum temperature of 52°C .^[38] Therefore, the use of plasmonic nanostructures in the design of hybrid nanomaterials for water steam generation is a promising field of research.

2.3. Catalytic Reduction of 4-Nitrophenol

To confirm the catalytic ability of the AuAg wNRs, we studied the water-soluble PEG-SH-AuAg wNRs (3) in the reduction of 4-nitrophenol (4-NP) to 4-aminophenol (4-AP) in the presence of an excess of NaBH_4 . The catalyzed conversion of 4-NP into 4-AP is important for practical applications. One of them is focused to the environmental remediation of nitroaromatic compounds,^[39] which are known pollutants. Another application is that the obtained reaction 4-AP product is a starting material involved in the synthesis of valuable pharmaceuticals such as, for example, paracetamol.^[40]

The catalytic activity was monitored through the UV-vis spectral changes between a decreasing 4-NP and increasing 4-AP absorption bands over time.

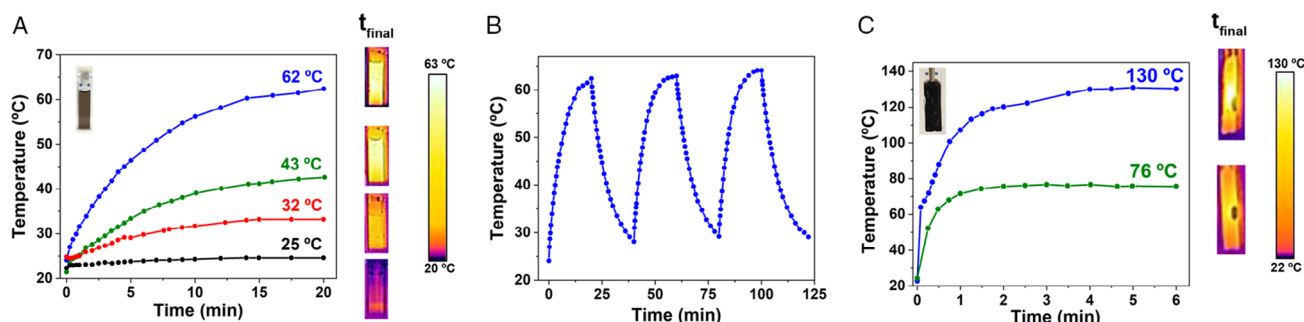


Figure 6. A) Temperature increase of aqueous solution of PEG-SH-AuAg wNRs (3) (3.3 mg mL^{-1}) using 850 nm (red) or 940 nm (blue) NIR LEDs and temperature increase of free solvent with 850 nm (black) and 940 nm (green) LEDs. B) Photothermal heating and cooling cycles for PEG-SH-AuAg wNRs (3) using 940 nm NIR LEDs. C) Temperature increase of a PMMA film of OA-AuAg NRs (1) with 850 nm (green) and 940 nm (blue).

As shown in Figure 7, the degradation of 4-NP was very fast (2.5 min) and without an induction period, demonstrating the excellent interaction between 4-NP and NaBH₄ reactants with the wNRs surface, despite the presence of a stabilizing PEG-SH polymeric shell. The representation of ln(A_t/A₀) versus time (s) plot for 3 displays a one-step reduction mechanism presenting a pseudo-first-order kinetics with kinetic constant $k_{app} = 3.0 \times 10^{-2} \text{ s}^{-1}$ giving a quantitative 4-NP conversion. This catalytic conversion rate is faster than the one recently reported by some of us for core@satellites Prussian Blue Analogue@Au-Ag nanoparticles ($9.3 \times 10^{-3} \text{ s}^{-1}$), where both the bimetallic plasmonic nanoparticles and the Prussian Blue Analogue display catalytic activity toward the plasmonic-assisted reduction of 4-NP.^[41]

In addition, the activation energy (E_a) of the reduction of 4-NP to 4-AP catalyzed by water-soluble PEG-SH-AuAg wNRs (3) was calculated. For this, an estimation of the kinetic constant k_{app} at different temperatures in the 25–40 °C range and the use of the Arrhenius equation (see Supporting Information) provides a E_a value of 59.0 kJ mol⁻¹. This value is similar to previously reported ones for bimetallic AuAg NPs stabilized with Pluronic F127 between 51–70 kJ mol⁻¹,^[42] and also comparable to the ones obtained for chitosan-stabilized bimetallic AuAg NPs of different metallic compositions with values between 27 and 58 kJ mol⁻¹.^[43]

2.4. Plasmon-Induced Catalytic Reduction of 4-Nitrostyrene

In view of the excellent optical and catalytic properties of AuAg wNRs, we wondered about taking advantage of the intense I-SPR

absorptions displayed by these singular nanostructures to improve the efficiency of industrially demanding processes in plasmonic-assisted catalytic transformations. In this context, we have studied the selective reduction of nitroaromatics to functional amines in the presence of C=C groups that leads to interesting intermediates as, for instance, in pharmaceuticals or chemical product synthesis. The selectivity in the catalytic transformations is usually concomitant with the loss of activity.^[44] Therefore, the design of efficient and selective catalysts is a challenging issue.

The reduction of 4-nitrostyrene was carried out using NH₃·BH₃ as reducing agent in methanol as solvent (Figure 8). Table in Figure 8 displays the results of this catalytic reaction in the dark during 1 h, showing a quite low conversion of 35% with a high selectivity toward the reduction of the nitro to amino group, keeping the double bond group almost unaltered. Very interestingly, the photocatalytic reduction of 4-nitrostyrene using LED NIR (940 nm) irradiation during 1 h in the presence of 3 led to a complete conversion, keeping a very high selectivity toward the formation of 4-aminostyrene.

It is worth mentioning that the NIR irradiation does not lead to a measurable temperature increase because the amount of PEG-SH-AuAg wNRs (3) used in the process was very small, discarding a macroscopic photothermal heating as responsible for this transformation. This result is similar to that previously reported for Au-based NP multishell structures, which showed a similar behavior in this catalytic transformation but using visible light. In our case, the NIR plasmonic-assisted reduction of 4-nitrostyrene would arise from the surface plasmon decay generation of hot electrons on the AuAg wNRs surface, although

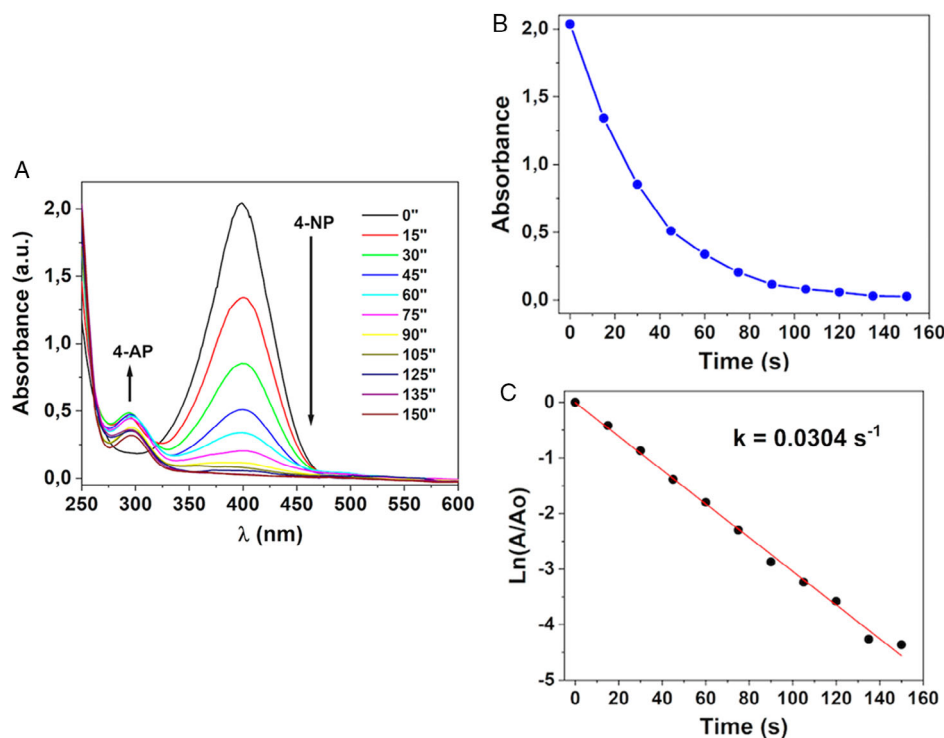


Figure 7. A) Time-dependent UV-vis absorption spectra of 4-NP (400 nm) and 4-AP (295 nm) during the catalyzed reduction by 3. B) Plot of absorbance of 4-NP as a function of time and C) plot of ln(A/A₀) as a function of time.

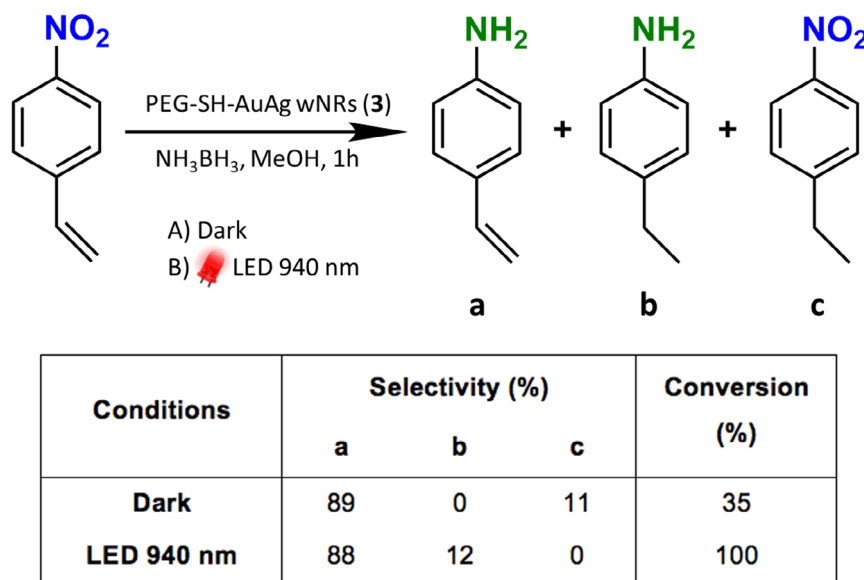


Figure 8. Selective hydrogenation of 4-nitrostyrene using PEG-SH-AuAg wNRs (3) as catalyst in the dark and under NIR LED light (940 nm) irradiation.

photothermal contributions via localized wNRs surface temperature increase cannot be ruled out.^[45,46] At this point, it is important to highlight that bare gold NR-enabled photocatalysis is a relatively rare phenomena,^[1,47] being gold-NR/semiconductor systems much more common. Indeed, the AuAg wNRs system is competitive in the selective reduction of 4-aminostyrene to aminostyrene with more complex heterostructured systems such as 1) Cu NPs deposited on carbon quantum dots (CDs) that act as photocatalyst in this reaction under visible light;^[48] 2) Cu₃P-CDs-Cu multicomponent photocatalytic system, which achieves a high selectivity in the reduction of 4-nitrostyrene to 4-aminostyrene in short times;^[49] or 3) platinum clusters deposited on Bi₂MoO₆ nanosheet surfaces that produce a 100% selectivity for this reduction and a complete conversion in the presence of visible light.^[50]

2.5. Plasmonic and Photothermally Induced Catalytic Ammonia Borane Dehydrogenation

Considering the very good performance of AuAg wNRs as plasmonic photocatalysts and photothermal heating nanostructures, we also studied the ammonia borane dehydrogenation process. The compound NH₃·BH₃ is an excellent, safe, and cheap H₂ storage material (up to 19.6 wt%), what makes it ideal for its use in hydrogen energy applications. In addition, a controlled and efficient production of H₂ through the hydrolysis of NH₃·BH₃ is an important prerequisite for the design of potential applications.^[51,52] Few previous works have dealt with the plasmonic-induced photocatalytic ammonia borane dehydrogenation. Among them, Au NPs dumbbell-like nanostructures show an efficient H₂ production from ammonia borane under visible light irradiation.^[53] More complex silver-based plasmonic heterostructures have also performed efficiently in this dehydrogenation reaction. For instance, Ag NPs displaying different aspect ratios were synthesized within mesoporous SBA-15,^[54] or within titanium-containing mesoporous SBA-15,^[55] leading

to enhanced plasmonic photocatalytic dehydrogenation performance under visible light ($\lambda > 420$ nm) or UV-vis light, respectively. More recently, plasmonic Ag@Pd nanocubes have been used for this transformation taking advantage of the light harvesting properties of the plasmonic silver component and the catalytic activity of the palladium shell.^[52]

At this point, plasmonic photocatalysis using NIR-active nanostructures constitutes a smart approach for the improvement of the efficiency of this hydrolytic process. Indeed, both the surface plasmon-induced generation of hot electrons and the photothermal heating achieved upon NIR LED light irradiation of the PEG-SH-AuAg wNRs (3) contribute to the H₂ release improvement in the hydrolysis of NH₃·BH₃. To show this dual mechanism, we have carried out a series of experiments. We have used a two-neck flask with a septum cap and a connection to a pressure sensor and a data transmitter (see Supporting Information for details).

With this device, we can detect the pressure increase during the NH₃·BH₃ hydrolytic dehydrogenation. The H₂ (or water steam) evolution rate can also be determined (bar min⁻¹) by the linear fitting of the H₂ (or water steam) evolution curve in the first minutes, where a linear pressure increase is observed. In order to take into account the pressure increase arising from water steam formation when the temperature raises, we carried out the irradiation of a 5 mL water solution including 8 mg of PEG-SH-AuAg wNRs (3) (pink line in **Figure 9**). The plasmonic photothermal heating increased the temperature of the solution up to 50 °C and also increased the pressure in the device up to 0.085 bar (water steam evolution rate of 0.0049 bar min⁻¹). In another experiment, we tested the degradation of NH₃·BH₃ in 5 mL water solution thermally heated at 50 °C and in the absence of AuAg wNRs. In this experiment, the pressure increases up to 0.13 bar (H₂ and water steam of 0.0064 bar min⁻¹), indicating an approximate H₂ release of 0.05 bar, in addition to the water steam produced at 50 °C heating (blue line in **Figure 9**). In a next experiment, we observed the catalytic dehydrogenation of NH₃·BH₃ in

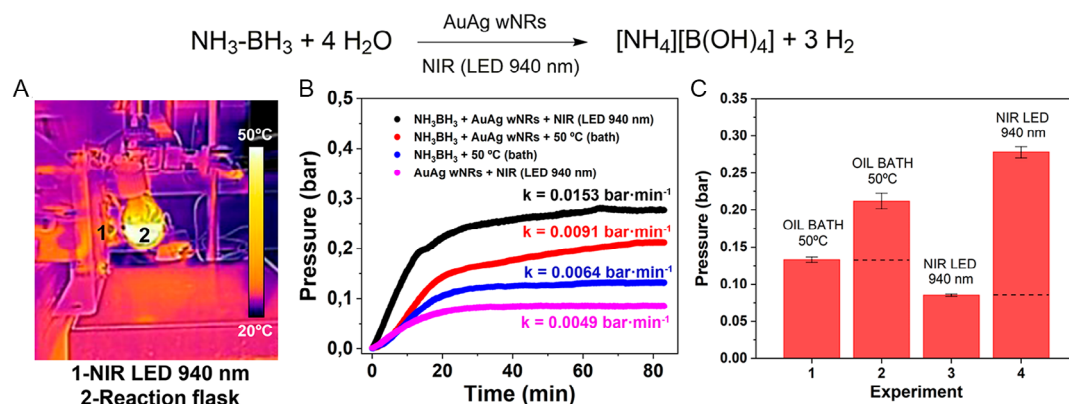


Figure 9. A) Thermographic images showing the increase of the temperature in the flask upon irradiation with a NIR LED of 940 nm wavelength; B) plot of evolved H_2 with time for the $\text{NH}_3\text{-BH}_3$ dehydrogenation under thermal conditions without catalyst (blue); under thermal conditions in the presence of AuAg wNRs 3 catalyst (red) and under NIR (940 nm) irradiation in the presence of AuAg wNRs 3 catalyst (black). The pink line represents the water steam evolution arising from the photothermal heating of the AuAg wNRs; C) graphical bar representation of each experiment showing the different contributions to the pressure increase. Experiments 1 and 2 show thermal conditions results and experiments 2 and 3 show photothermal conditions results, respectively.

the presence of PEG-SH-AuAg wNRs (3) at 50 °C in the absence of NIR light irradiation. In this case, the pressure increases up to 0.21 bar (H_2 and water steam evolution rate of 0.0091 bar min^{-1}), in agreement with a metal catalysed dehydrogenation, producing ≈ 0.12 bar of H_2 by subtracting the water steam pressure (red line in Figure 9). Finally, in an additional experiment we measured a pressure increase up to 0.28 bar (H_2 and water steam evolution rate of 0.0153 bar min^{-1}) when the $\text{NH}_3\text{-BH}_3$ dehydrogenation was performed in the presence of AuAg wNRs (3) and under NIR LED light irradiation of 940 nm (black line in Figure 9). The additional 0.15 bar increase of released H_2 with respect to the experiment performed in the dark at 50 °C and in the absence of AuAg wNRs arises from both plasmonically induced generation of hot electrons and photothermal heating because this last experiment reaches 50 °C due to the plasmonic NIR absorption. The column bar graphic depicted in Figure 9 summarizes the results organized in thermal (exp. 1 and 2) and photothermal dehydrogenation results (exp. 3 and 4). Experiments 1 and 2, performed under thermal conditions, show a H_2 pressure increase of 0.08 bar arising from the catalytic activity of the PEG-SH-AuAg wNRs (3) (experiment 2). However, when NIR LED light is employed (experiments 3 and 4) it is clearly observed that the plasmonically induced generation of hot electrons and photothermal heating produces an important increase of H_2 pressure of almost 0.2 bar (experiment 4). Therefore, these results show the very good performance of these AuAg wNRs for H_2 release in the photocatalytic/photothermal dehydrogenation of ammonia borane. Overall, the use of plasmonic photocatalyst such as NIR-active AuAg wNRs could be important for the design of practical applications by the use of renewable source of energy, i.e., NIR part of solar light, for the generation of sustainable hydrogen energy stocked in easy-to-use solid storage systems.

3. Conclusion

In conclusion, we have described a one-step method for the synthesis of wavy AuAg NRs of small size and controlled aspect

ratios, by the mild decomposition of an organometallic Au(I)–Ag(I) complex in THF solution and in the presence of OA as growth-directing agent and stabilizing ligand. These AuAg wNRs display tuneable length-dependent plasmonic properties in the NIR II region arising from the longitudinal mode of the LSPR (l-LSPR) absorption. The OA exchange by L-glutathione (GSH) or poly(ethylene glycol) methyl ether thiol (PEG-SH) leads to the formation of hydrophilic nanostructures that can be easily handled both in solid state and in water solution. The AuAg wNRs display NIR LED light-induced photothermal heating and interesting catalytic properties in the reduction of 4-nitrophenol to 4-aminophenol. The intense plasmonic absorption of these wNRs in the NIR range has also allowed their use in the selective photocatalytic reduction of 4-nitrostyrene, being a rare example of photocatalytic plasmonic NRs. In addition, the water-soluble PEG-SH-AuAg wNRs (3) have been used as plasmonic photocatalyst in the dehydrogenation of $\text{NH}_3\text{-BH}_3$ for H_2 release.

We envision that these plasmonic AuAg wNRs nanostructures constitute an interesting material for improved photothermal and photocatalytic applications.

4. Experimental Section

General: The complex $[\text{Au}_2\text{Ag}_2(\text{C}_6\text{F}_5)_4(\text{Et}_2\text{O})_2]_n$ was synthesized according to published procedure.^[56] OA was obtained from Sigma-Aldrich, with 90% of purity, and used as received. Reactions were carried out under argon atmosphere, and AuAg wNRs were isolated by centrifugation, washing first with 1:1 toluene:ethanol mixture and then twice with 2:1 toluene:ethanol mixture. All experiments were repeated at least twice to check the reproducibility of the synthetic route.

Instrumentation: UV/vis/NIR spectra were recorded with a Shimadzu UV-3600 UV-vis-NIR spectrophotometer and UV-vis spectra were recorded with a Hewlett Packard 8453 Diode Array UV-vis spectrophotometer. Samples for TEM were directly drop-casted from THF or water dispersions (2–3 drops) over carbon-coated Cu grids. TEM images were obtained with a JEOL JEM 2100 or a Tecnai T20 microscope. For crystal structure determination and atomic resolution imaging of AuAg wNRs, selected samples were analyzed by HRTEM using a JEOL JEM 2100-F

microscope, equipped with a Schottky field emission electron source, and operating at 200 kV. The same microscope was used in STEM mode and bright field geometry, providing an electron probe of 1 nm, to perform EDS spectra. The latter were collected by using a Bruker X-Flash Silicon Drift detector, with active area of 30 mm². For the EDS spectrum analysis, the Cliff–Lorimer quantification method was used, linearly modeling the small background contribution to subtract, and using a Gaussian function to model both Ag-L α and Au-L α . The LED system used for photothermal heating experiments and for plasmonic-assisted synthesis consisted of one, 3.75 W NIR LedEngin LZ4-00R608 of 850 nm wavelength or a 3.75 W NIR LedEngin LZ4-00R708 of 940 nm wavelength attached to a homemade air-cooled aluminum heat sink device. The photothermal temperature increase in the different experiments was measured with a FLIR E6-XT IR thermographic camera. XPS experiments were performed in a Kratos AXIS Supra spectrometer, using a monochromatized Al K α source (1486.6 eV) operating at 12 kV and 10 mA. Wide scans were acquired at analyzer pass energy of 160 eV, whereas high-resolution narrow scans were performed at constant pass energy of 20 eV and steps of 0.1 eV. The photoelectrons were detected at a take-off angle of $F = 0^\circ$ with respect to the surface normal. Basal pressure in the analysis chamber was less than 5×10^{-9} Torr. The spectra were obtained at room temperature. The binding energy (BE) scale was internally referenced to the C 1s peak (BE for C–C = 284.9 eV). GC/MS measurements were carried out using an Agilent Technologies Gas Chromatograph model 7890 with mass detector model 5977B MSD. H₂ release experiments were performed using a ManontheMoonTech Series X103 device, which consist of a 2-neck flask with a septum cap and the other output connected to a pressure sensor and a data transmitter.

Synthesis of OA-AuAg wNRs (1): [Au₂Ag₂(C₆F₅)₄(Et₂O)₂]_n (20 mg, 0.014 mmol) was dissolved in anhydrous THF (30 mL) under argon atmosphere and 64 equivalents of OA (283 mg, 0.9 mmol) were added. The mixture was light-protected and stirred under reflux conditions (66 °C) for 6 h, leading to a dark red solution. The solvent was removed under vacuum and the dark solid obtained was washed by centrifugation, once with 1:1 toluene:ethanol mixture (20 mL), and then, twice with 2:1 toluene:ethanol mixture (15 mL). Finally, the solid was dissolved in THF, forming a brown solution, for UV/vis/NIR spectrum and TEM sampling.

Synthesis of GSH-AuAg wNRs (2): OA-AuAg wNRs (1) was dissolved in THF (5 mL) and a water solution of reduced L-glutathione (25 mg in 5 mL) was added. The mixture was stirred for 30 min at room temperature. Then, THF was removed under vacuum and the resulting brown water solution was lyophilized during 2 days, resulting a dark brown solid. This solid was dissolved in water for TEM sampling or in DMSO for UV/vis/NIR analysis.

Synthesis of PEG-SH-AuAg wNRs (3): OA-AuAg wNRs (1) was dissolved in THF (5 mL) and a water solution of poly(ethylene glycol) methyl ether thiol (25 mg in 5 mL) was added. The resulting mixture was stirred for 30 min at room temperature and then THF was removed under vacuum. The resulting water solution was lyophilized during 2 days, resulting a dark brown solid. This solid was dissolved in water for TEM sampling or in DMSO for UV/vis/NIR spectrum.

Synthesis of OA-AuAg wNRs (4-8): [Au₂Ag₂(C₆F₅)₄(Et₂O)₂]_n (20 mg, 0.014 mmol) was dissolved in anhydrous THF (30 mL) under argon atmosphere and different amounts of OA were added for each nanostructure (see Table S1, Supporting Information). For each reaction, the mixture was light-protected and stirred under reflux conditions (66 °C) for 6 h, leading to a dark red solution. The solvent was removed under vacuum and the dark solid obtained was washed by centrifugation, once with 1:1 toluene:ethanol mixture (20 mL), and then twice with 2:1 toluene:ethanol mixture (15 mL). Finally, the solid was dissolved in THF, forming a brown solution, for UV/vis/NIR spectrum and TEM sampling.

Catalysis: 4-Nitrophenol to 4-Aminophenol: In a standard quartz cuvette with 2.5 mL of distilled water and 125 μ L of a 4-nitrophenol solution (2.5×10^{-3} M), 150 μ L of a NaBH₄ (1 M) was added forming the corresponding 4-nitrophenolate bright yellow solution. Then, 100 μ L of a PEG-SH-AuAg wNRs (3) solution (5 mg in 0.5 mL of water) was added and the UV absorption band with a maximum around 400 nm corresponding to 4-nitrophenolate was monitored each 15 s.

Photocatalytic Reduction of 4-Nitrostyrene to 4-Aminostyrene: 4-Nitrostyrene (30 mg, 0.2 mmol) was dissolved in 2 mL of methanol with PEG-SH-AuAg wNRs (3) (5 mg). This solution was transferred into a Schlenk tube and then 0.6 mL of a methanol solution of NH₃·BH₃ (15 mg, 0.5 mmol) was added. The mixture was stirred during 1 h under dark conditions or under 940 nm LED NIR light irradiation at room temperature. The resulting solution was filtered with a 0.22 μ m nylon filter and extracted with a mixture solution of CHCl₃ and water (5:1), discarding the water phase. Finally, the organic phase was analyzed through GC–MS.

Plasmonic and Photothermally Induced Catalytic NH₃·BH₃ Dehydrogenation: In each experiment, NH₃·BH₃ 5 mL water solutions (or water) were kept under vacuum during 30 min and then PEG-SH-AuAg wNRs (3) 0.5 mL water solutions were injected. Then, 940 nm NIR LED or temperature control (oil bath) was connected and the pressure was monitored until stabilization. The temperature of the oil bath was set to 50 °C because the solution with nanoparticles under 940 nm LED light irradiation reaches this same temperature.

Supporting Information

Supporting Information is available from the Wiley Online Library or from the author.

Acknowledgements

Grant PID2019-104379RB-C22 funded by MCIN/AEI/10.13039/501100011033 and by “ERDF A way of making Europe” and the EC for financial support through the FEDER POCTEFA project NUTRIA (EFA 356/19) are acknowledged for financial support. J.Q. also acknowledges MECO for a FPU grant. The authors thank the SERMET-Universidad de Cantabria. The authors also acknowledge the use of instrumentation as well as the technical advice provided by the National Facility ELECMI ICTS, node “Laboratorio de Microscopias Avanzadas” at Universidad de Zaragoza.

Conflict of Interest

The authors declare no conflict of interest.

Data Availability Statement

The data that support the findings of this study are available in the supplementary material of this article.

Keywords

gold, nanorods, photothermal heating, plasmonic catalysis, silver

Received: August 25, 2022

Revised: September 5, 2022

Published online: October 2, 2022

- [1] J. Zheng, X. Cheng, H. Zhang, X. Bai, R. Ai, L. Shao, J. Wang, *Chem. Rev.* **2021**, *121*, 13342.
- [2] X. Zhuo, M. Henriksen-Lacey, D. Jimenez de Aberasturi, A. Sánchez-Iglesias, L. M. Liz-Marzán, *Chem. Mater.* **2020**, *32*, 5879.
- [3] L. Wang, Y. Zhu, L. Xu, W. Chen, H. Kuang, L. Liu, A. Agarwal, C. Xu, N. A. Kotov, *Angew. Chem., Int. Ed.* **2010**, *49*, 5472.
- [4] L. Vigderman, B. P. Khanal, E. R. Zubarev, *Adv. Mater.* **2012**, *24*, 4811.
- [5] P. Zijlstra, J. W. M. Chon, M. Gu, *Nature* **2009**, *459*, 410.

- [6] N. S. Abadeer, C. J. Murphy, *J. Phys. Chem. C* **2016**, *120*, 4691.
- [7] Y. Khalavka, J. Becker, C. Sönnichsen, *J. Am. Chem. Soc.* **2009**, *131*, 1871.
- [8] S. Linic, U. Aslam, C. Boerigter, M. Morabito, *Nat. Mater.* **2015**, *14*, 567.
- [9] H. Y. Xu, C. X. Kan, C. Z. Miao, C. S. Wang, J. J. Wei, Y. Ni, B. B. Lu, D. N. Shi, *Photon. Res.* **2017**, *5*, 27.
- [10] N. D. Burrows, S. Harvey, F. A. Idesis, C. J. Murphy, *Langmuir* **2017**, *33*, 1891.
- [11] K. D. Gilroy, A. Ruditskiy, H.-C. Peng, D. Qin, Y. N. Xia, *Chem. Rev.* **2016**, *116*, 10414.
- [12] W. H. Qi, S. T. Lee, *J. Phys. Chem. C* **2010**, *114*, 9580.
- [13] Y. Ni, C. Kan, L. He, X. Zhu, M. Jiang, D. Shi, *Photonics Res.* **2019**, *7*, 558.
- [14] W. Albrecht, J. E. S. van der Hoeven, T.-S. Deng, P. E. de Jongh, A. van Blaaderen, *Nanoscale* **2017**, *9*, 2845.
- [15] Y. Bai, C. Gao, Y. Yin, *Nanoscale* **2017**, *9*, 14875.
- [16] S. Ke, C. Kan, X. Zhu, C. Wang, W. Gao, Z. Li, X. Zhu, D. Shi, *J. Mater. Sci. Technol.* **2021**, *91*, 262.
- [17] M. Cao, Q. Liu, M. Chen, L. Chen, D. Yang, H. Hu, L. He, G. Zhang, Q. Zhang, *ACS Omega* **2018**, *3*, 18623.
- [18] J. Huang, Y. Zhu, C. Liu, Y. Zhao, Z. Liu, M. Nejjib Hedhili, A. Fratolocchi, Y. Han, *Small* **2015**, *11*, 5214.
- [19] R. Takahata, S. Yamazoe, K. Koyasu, T. Tsukuda, *J. Am. Chem. Soc.* **2014**, *136*, 8489.
- [20] J. Crespo, J. M. López-de-Luzuriaga, M. Monge, M. Elena Olmos, M. Rodríguez-Castillo, B. Cormary, K. Soulantica, M. Sestu, A. Falqui, *Chem. Commun.* **2015**, *51*, 16691.
- [21] R. Takahata, S. Yamazoe, K. Koyasu, K. Imura, T. Tsukuda, *J. Am. Chem. Soc.* **2018**, *140*, 6640.
- [22] S. Gong, W. Schwab, Y. W. Wang, Y. Chen, Y. Tang, J. Si, B. Shirinzadeh, W. L. A. Cheng, *Nat. Commun.* **2014**, *5*, 3132.
- [23] H.-H. Chang, C. J. Murphy, *Chem. Mater.* **2018**, *30*, 1427.
- [24] T. Song, L. Tang, L. H. Tan, X. Wang, N. Sai, R. Satyavolu, H. Xing, Z. Wang, J. Li, H. Liang, Y. Lu, *Angew. Chem., Int. Ed.* **2015**, *54*, 8114.
- [25] Q. Zhang, Y. Zhou, E. Villarreal, Y. Lin, S. Zou, H. Wang, *Nano Lett.* **2015**, *15*, 4161.
- [26] T. Guo, Y. Tan, *Nanoscale* **2013**, *5*, 561.
- [27] J. Crespo, A. Falqui, J. García-Barrasa, J. M. López-de-Luzuriaga, M. Monge, M. E. Olmos, M. Rodríguez-Castillo, M. Sestu, K. Soulantica, *J. Mater. Chem. C* **2014**, *2*, 2975.
- [28] R. Yu, L. M. Liz-Marzán, F. J. García de Abajo, *Chem. Soc. Rev.* **2017**, *46*, 6710.
- [29] C. Zhu, H.-C. Peng, J. Zeng, J. Liu, Z. Gu, Y. Xia, *J. Am. Chem. Soc.* **2012**, *134*, 20234.
- [30] M. Caux, H. Menard, Y. M. AlSalik, J. T. S. Irvine, H. Idriss, *Phys. Chem. Chem. Phys.* **2019**, *21*, 15974.
- [31] T. Fujigaya, C. Kim, Y. Hamasaki, N. Nakashima, *Sci. Rep.* **2016**, *6*, 21314.
- [32] H. Haidari, N. I. Goswami, R. Bright, Z. Kopecki, A. J. Cowin, S. Garga, K. Vasilev, *Nanoscale Adv.* **2019**, *1*, 2365.
- [33] H. Han, J. Lee, D. W. Park, S. E. Shim, *Macromol. Res.* **2010**, *18*, 435.
- [34] Z. Song, W. Li, F. Niu, Y. Xu, L. Niu, W. Yang, Y. Wang, J. Liu, *J. Mater. Chem. A* **2017**, *5*, 230.
- [35] M. Dhiman, A. Maity, A. Das, R. Belgamwar, B. Chalke, Y. Lee, K. Sim, J.-M. Nam, V. Polshettiwar, *Chem. Sci.* **2019**, *10*, 6594.
- [36] L. Tian, J. Luan, K.-K. Liu, Q. Jiang, S. Tadeipalli, M. K. Gupta, R. R. Naik, S. Singamaneni, *Nano Lett.* **2016**, *16*, 609.
- [37] T. Wu, H. Li, M. Xie, S. Shen, W. Wang, M. Zhao, X. Mo, Y. Xia, *Mater. Today Energy* **2019**, *12*, 129.
- [38] J. Zhou, Y. Gu, Z. Deng, L. Miao, H. Su, P. Wang, J. Shi, *Sustain. Mater. Technol.* **2018**, *17*, e00090.
- [39] L. Qin, G. Zeng, C. Lai, D. Huang, C. Zhang, M. Cheng, H. Yi, X. Liu, C. Zhou, W. Xiong, F. Huang, W. Cao, *Sci. Total Environ.* **2019**, *652*, 93.
- [40] P. Zhao, X. Feng, D. Huang, G. Yang, D. Astruc, *Coord. Chem. Rev.* **2015**, *287*, 114.
- [41] E. Mamontova, M. Rodríguez-Castillo, E. Oliviero, Y. Guari, J. Larionova, M. Monge, J. Long, *Inorg. Chem. Front.* **2021**, *8*, 2248.
- [42] M. S. Holden, K. E. Nick, M. Hall, J. R. Milligan, Q. Chen, C. C. Perry, *RSC Adv.* **2014**, *4*, 52279.
- [43] A. Murugadoss, N. Kai, H. Sakurai, *Nanoscale* **2012**, *4*, 1280.
- [44] P. Serna, A. Corma, *ACS Catal.* **2015**, *5*, 7114.
- [45] J. Li, Y. Long, Y. Liu, L. Zhang, Q. Wang, X. Wang, S. Song, H. Zhang, *Angew. Chem., Int. Ed.* **2020**, *59*, 1103.
- [46] V. Jain, R. K. Kashyap, P. P. Pillai, *Adv. Opt. Mater.*, **2022**, 2200463.
- [47] S. Pal, A. Dutta, M. Paul, A. Chattopadhyay, *J. Phys. Chem. C* **2020**, *124*, 3204.
- [48] Y. Ren, C. Hao, Q. Chang, N. Li, J. Yangab, S. Hu, *Green Chem.* **2021**, *23*, 2938.
- [49] Y. Ren, C. Hao, Q. Chang, N. Li, J. Yangab, S. Hu, *J. Mater. Chem. A* **2021**, *9*, 25374.
- [50] Y. Shi, Z. Wang, C. Liu, T. Wu, R. Liu, L. Wu, *Appl. Catal. B: Environ.* **2022**, *304*, 121010.
- [51] C. D. Mboyi, D. Poinot, J. Roger, K. Fajerweg, M. L. Kahn, J.-C. Hierso, *Small* **2021**, *17*, 2102759.
- [52] P. Xu, W. Lu, J. Zhang, L. Zhang, *ACS Sustain. Chem. Eng.* **2020**, *8*, 12366.
- [53] M. Zhu, Y. Dai, W. Fu, Y. Wu, X. Zou, T. You, Y. Sun, *Nanotechnology* **2018**, *29*, 165707.
- [54] K. Fuku, R. Hayashi, S. Takakura, T. Kamegawa, K. Mori, H. Yamashita, *Angew. Chem., Int. Ed.* **2013**, *52*, 7446.
- [55] P. Verma, Y. Kuwahara, K. Mori, H. Yamashita, *Chem. Eur. J.* **2017**, *23*, 3616.
- [56] E. J. Fernández, J. M. López-de-Luzuriaga, M. Monge, M. E. Olmos, R. C. Puelles, A. Laguna, A. A. Mohamed, J. P. Fackler Jr, *Inorg. Chem.* **2008**, *46*, 8069.